Extended Hybrid Modulation for Multi-Stage Constant-Current Wireless EV Charging

Zhu, Gangwei; Zhang, Shibo; Deng, Zichen; Wang, Jundong; Li, Yongpeng; Dong, Jianning; Bauer, Pavol

DOI
10.1109/TPEL.2025.3549840

Publication date
2025

Document Version
Final published version

Published in
IEEE Transactions on Power Electronics

Citation (APA)
Zhu, G., Zhang, S., Deng, Z., Wang, J., Li, Y., Dong, J., & Bauer, P. (2025). Extended Hybrid Modulation for Multi-Stage Constant-Current Wireless EV Charging. *IEEE Transactions on Power Electronics*, *40*(7), 10095-10110. https://doi.org/10.1109/TPEL.2025.3549840

Extended Hybrid Modulation for Multistage Constant-Current Wireless EV Charging

Gangwei Zhu, *Graduate Student Member, IEEE*, Shibo Zhang, *Graduate Student Member, IEEE*, Zichen Deng, *Graduate Student Member, IEEE*, Jundong Wang, *Graduate Student Member, IEEE*, Yongpeng Li, *Graduate Student Member, IEEE*, Jianning Dong, *Senior Member, IEEE*, and Pavol Bauer, *Senior Member, IEEE*

***Abstract*—This article presents an extended hybrid modulation (EHM) technique to achieve multistage constant-current (MSCC) charging of electric vehicles using wireless power transfer (WPT) technology. Although most research focuses on constant-current constant-voltage charging, MSCC charging offers key advantages, such as lower temperature rise, decreased charging time, and prolonged battery lifespan. However, the existing phase-shift-modulation (PSM) method encounters substantial circulating reactive power and significant efficiency drops in MSCC charging. To overcome this, an EHM strategy is proposed to expand the modulation range of PSM. By applying EHM to both the inverter and active rectifier, the proposed method provides up to 16 operating modes to facilitate multiple CC outputs. Furthermore, an optimal mode trajectory, specifically designed for the MSCC charging, is developed. By implementing this trajectory across different charging stages, zero-voltage-switching is achieved for all power switches, and the overall power loss of the system is minimized. Finally, a WPT prototype was developed to validate the proposed approach. Experimental results demonstrate that the proposed approach effectively enables the MSCC charging while notably enhancing transmission efficiency, achieving dc-to-dc efficiencies between 92.45% and 95.67% across a power range of 231 to 3.015 kW.**

***Index Terms*—Extended hybrid modulation (EHM), multistage constant-current (MSCC) charging, wireless power transfer (WPT).**

I. Introduction

THE electric vehicle (EV) market has seen significant expansion, highlighting the urgent need for advanced EV charging infrastructures. Currently, EVs primarily employ conductive charging technology, which demands drivers to handle and connect charging cables manually. To streamline the intricacy of connecting bulky cables, wireless power transfer (WPT) technology emerges as a more user-friendly alternative, delivering weather-proof, hands-free, and autonomous charging solutions for EVs [1].

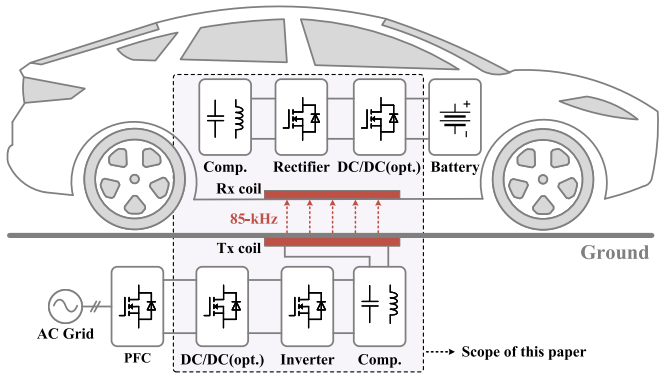

Fig. 1. Typical architecture of wireless EV charging systems.

Fig. 1 illustrates the typical architecture of wireless EV charging systems, where batteries function as the load. To achieve complete battery charging, the constant-current and constant-voltage (CC-CV) charging solution is commonly adopted. Nevertheless, achieving simultaneous load-independent CC and CV outputs in wireless EV chargers remains challenging and often necessitates complex solutions. One approach investigated involves using two distinct switching frequencies to enable CC and CV outputs [2], [3], [4]. However, these methods are not preferred in industrial standards, such as SAEJ 2954 [5], due to the broad frequency tuning range required. Alternatively, hybrid compensation topologies have been extensively studied to achieve both CC and CV outputs [6], [7], [8]. Nonetheless, these topologies necessitate extra reconfigurable passive components and relays for topology reconstruction, which notably increases system complexity and reduces power density. In addition to the challenges of achieving simultaneous CC and CV outputs, another disadvantage of CC-CV charging lies in its potential adverse impact on battery lifespan due to continuous structural stress [9]. As an alternative, the multistage constant-current (MSCC) charging strategy offers some key advantages. Compared to the CC-CV profile, the MSCC strategy requires only

Received 22 October 2024; revised 25 January 2025; accepted 1 March 2025. Date of publication 11 March 2025; date of current version 14 April 2025. This work was supported in part by the China Scholarship Council (CSC) under Grant 202106230112 and in part by the CSC. Recommended for publication by Associate Editor C. Fernandez. *(Corresponding authors: Shibo Zhang; Zichen Deng.)*

The authors are with the DC System, Energy Conversion and Storage (DCE&S) Group, Faculty of Electrical Engineering, Mathematics and Computer Science (EEMCS), Delft University of Technology, 2624 CP Delft, The Netherlands (e-mail: g.zhu-2@tudelft.nl; s.zhang-6@tudelft.nl; z.deng-4@tudelft.nl; j.wang-16@tudelft.nl; y.li-23@tudelft.nl; j.dong-4@tudelft.nl; p.bauer@tudelft.nl).

Color versions of one or more figures in this article are available at https://doi.org/10.1109/TPEL.2025.3549840.

Digital Object Identifier 10.1109/TPEL.2025.3549840

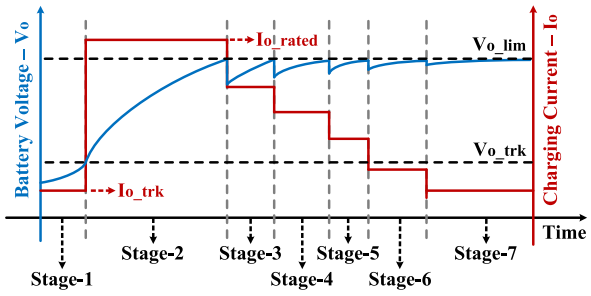

Fig. 2. Typical seven-stage MSCC charging profile for EV batteries [13].

several CC outputs, thereby reducing the complexity of achieving the targeted charging profile [10], [11]. More importantly, the MSCC charging contributes to lower temperature rise, reduced charging time, and extended battery lifespan [12]. Fig. 2 demonstrates a typical seven-stage MSCC charging profile for EV batteries [13]. As illustrated in Fig. 2, the MSCC approach involves varying magnitudes of charging currents across multiple stages. The transition criteria between different stages depends on the battery-end voltage V_o. Initially, for deeply discharged batteries, a trickle charging stage is required (denoted as stage-1 in Fig. 2). During this stage, a trickle charging current I_{o_trk} is applied until V_o reaches the trickle voltage boundary V_{o_trk}. Typically, I_{o_trk} is set to a notably low value (approximately 0.05–0.2 times the rated charging current I_{o_rated} [14]) to precharge the battery and extend its lifespan. Following the trickle charging stage, the charging process transitions through multiple stages (stage-2 to stage-7). In these stages, the process proceeds to the next stage once the battery voltage reaches the voltage boundary V_{o_lim}.

In wireless EV charging, the equivalent battery load exhibits substantial variations. Therefore, to attain the desired charging profile, it is essential for the system to accommodate a wide load range. Existing research on wireless EV charging primarily focuses on the CC-CV charging profile. One approach to achieving wide output capability involves incorporating additional dc–dc converters [15], [16], as shown in Fig. 1. However, these extra power conversion stages result in additional power losses and components. To obviate the requirement for dc–dc converters, an alternative approach is to implement phase shift modulation (PSM) for the inverter and active rectifier [17], [18], [19]. Nonetheless, the PSM method poses challenges in achieving zero-voltage-switching (ZVS) under varying load conditions. In [20], a triple-phase-shift control strategy was proposed to facilitate wide-range ZVS. This approach introduces the phase difference between the inverter and the active rectifier as a new control variable for implementing ZVS. However, it leads to substantial reactive power at light-load conditions. To address this issue, a hybrid modulation (HM) approach was proposed, incorporating both full-bridge (FB) and half-bridge (HB) modes to facilitate ZVS under load variations [21], [22], [23]. Nevertheless, during the trickle charging stage of EV batteries, where the charging current is exceptionally low, this HM fails to minimize reactive power due to the limited tuning range of the HB mode. In addition, researchers have investigated alternative control variables to facilitate ZVS and achieve a wide operating range. These alternatives include varying the system operating frequency [24], [25], and the implementation of switch-controlled capacitors (SCCs) [26], [27]. Although these methods can effectively support wide output regulation and ZVS, they have notable drawbacks. Specifically, frequency adjustments are prone to bifurcation phenomena [28], which can cause significant system detuning, while the SCC technique necessitates extra power switches, consequently increasing both system complexity and cost.

On the other hand, recognizing the advantages of MSCC charging, some researchers have begun exploring its application in wireless charging. In [13], a multiharmonic power transmission technique was proposed to enable various CC outputs. However, this method only considers primary inverter control, resulting in constrained regulation capability compared to dual-side control. Moreover, it fails to achieve precise output current tracking. In [14], a reconfigurable rectifier was introduced to enable multiple constant current (CC) outputs, but this approach requires a significantly higher number of power switches and components. In [29], an optimal bivariate control strategy was proposed, incorporating a variable inductor and a secondary semiactive rectifier to achieve both ZVS and multiple CC outputs. Nonetheless, this method increases hardware complexity due to the additional variable inductor.

Based on the above-mentioned discussion, existing research on wireless MSCC charging is limited and reveals several limitations. To address these challenges, this article proposes an extended hybrid modulation-based dual-side control (EHM-DSC) approach for wireless MSCC charging of EVs. The main contributions of the proposed approach are summarized as follows.

1) The proposed approach achieves MSCC charging without the need for additional dc–dc converters or extra hardware circuits.
2) An EHM technique is introduced to expand the modulation tuning range of PSM. Furthermore, by applying EHM to both the inverter and active rectifier, the proposed method significantly improves the system's output regulation capability, facilitating the generation of multiple CC outputs for MSCC charging.
3) A unified ZVS model and a comprehensive power loss analysis methodology are developed for the proposed approach.
4) An optimal mode determination method, specifically designed for the MSCC charging profile, is developed. By implementing the optimal mode trajectory, ZVS for all power switches is achieved, and the overall power loss of the system is minimized.

The rest of this article is organized as follows. Section II illustrates the basic characteristics of WPT systems for MSCC charging. Furthermore, Section III elaborates on the proposed EHM-DSC method, while Section IV presents the experimental results. Finally, Section V concludes this article.

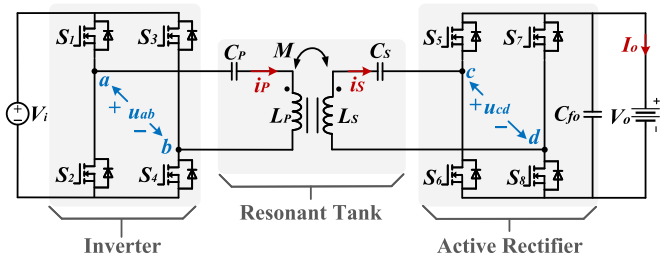

Fig. 3. Circuit topology of the SS-compensated WPT system.

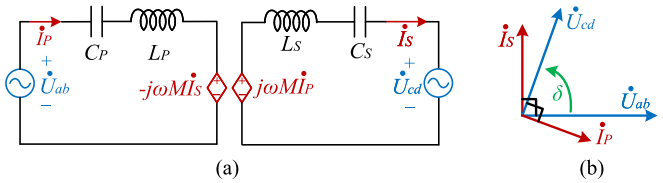

Fig. 4. (a) Ac equivalent circuit model, and (b) phasor diagram of the system based on the FHA approach.

II. WPT System for MSCC Charging

A. System Configurations

Fig. 3 illustrates the circuit topology of a typical WPT system featuring a series–series (SS) compensation network. This system configuration comprises a primary-side FB inverter, an SS-compensated resonant tank, a secondary-side FB active rectifier, and a dc output filter capacitor (C_{fo}). Within the SS-compensated resonant tank, L_P and L_S represent the self-inductances of the primary and secondary coils, while C_P and C_S are their compensation capacitors; M represents the mutual inductance between the primary and secondary coils. Moreover, in this system, the inverter output voltage and the rectifier input voltage are denoted by u_{ab} and u_{cd}, while the primary and secondary coil currents are expressed as i_P and i_S. In addition, the dc input voltage, the dc output voltage, and the dc output current of the system are indicated by V_i, V_o, and I_o, respectively.

Owing to the bandpass filtering characteristic of the SS-compensated resonant tank, the ac equivalent circuit model of the system can be established using the fundamental harmonic analysis (FHA) method, as illustrated in Fig. 4(a). Moreover, applying Kirchhoff's voltage law (KVL), the basic circuit equations of the system are derived as follows:

$$\begin{cases} \dot{U}_{ab} = (j\omega L_P + \frac{1}{j\omega C_P})\dot{I}_P - j\omega M\dot{I}_S \\ \dot{U}_{cd} = -(j\omega L_S + \frac{1}{j\omega C_S})\dot{I}_S + j\omega M\dot{I}_P \end{cases} \tag{1}$$

where $\dot{U}_{ab}$, $\dot{U}_{cd}$, $\dot{I}_P$, and $\dot{I}_S$ represent the phasor forms of the fundamental components in u_{ab}, u_{cd}, i_P, and i_S, respectively; ω denotes the switching frequency. Moreover, to address significant self-inductances of the loosely coupled coils, the compensation capacitors are designed as

$$C_P = 1/(\omega L_P), C_S = 1/(\omega L_S). \tag{2}$$

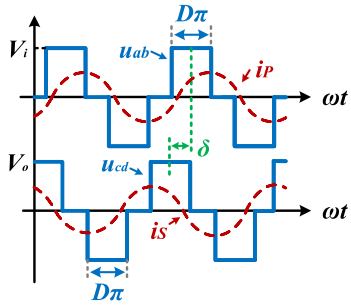

Fig. 5. Typical operating waveforms of the conventional PSM technique.

Substituting (2) into (1) yields

$$\dot{U}_{ab} \approx -j\omega M\dot{I}_S, \dot{U}_{cd} \approx j\omega M\dot{I}_P. \tag{3}$$

Based on (3), the phasor diagram of the system is illustrated in Fig. 4(b). Moreover, according to [20], the output power and the circulating reactive power of the system are formulated as

$$P_{\text{out}} = \text{Re}\{\dot{U}_{cd}\dot{I}_S^*\} = \frac{|\dot{U}_{ab}||\dot{U}_{cd}|\sin(\delta)}{\omega M} \tag{4}$$

$$Q_{\text{cir}} = \text{Im}\{\dot{U}_{cd}\dot{I}_S^*\} = -\frac{|\dot{U}_{ab}||\dot{U}_{cd}|\cos(\delta)}{\omega M}. \tag{5}$$

Substituting (4) into (5) obtains

$$|Q_{\text{cir}}| = P_{\text{out}}/\tan(\delta). \tag{6}$$

As indicated by (6), the circulating reactive power within the system is inversely related to the phase difference angle δ. In other words, for a constant output power, a larger value of δ corresponds to a lower reactive power.

B. Output Analysis and ZVS Implementation

To achieve the MSCC charging profile, it is imperative for the system to generate varying magnitudes of dc output current (I_o) across different charging stages. Given that the input voltage of the system (V_i) remains fixed, the PSM method can be employed to produce these varying output current magnitudes. Fig. 5 illustrates typical operating waveforms using the conventional PSM technique. Herein, the duty cycle of u_{ab} and u_{cd} is denoted by D, while the phase difference angle between u_{ab} and u_{cd} is represented by δ. According to the operating waveforms in Fig. 5, the phasor expressions of $\dot{U}_{ab}$ and $\dot{U}_{cd}$ are given by

$$\begin{cases} \dot{U}_{ab} = G_{U\_\text{inv}}V_i\sin(\frac{D\pi}{2})\angle 0 \\ \dot{U}_{cd} = G_{U\_\text{rec}}V_o\sin(\frac{D\pi}{2})\angle\delta \end{cases} \tag{7}$$

where G_{U_inv} and G_{U_rec} represent the dc to ac voltage gains of the inverter and rectifier at the full duty cycle ($D = 1$). Furthermore, by synthesizing (1), (2), and (7), the dc output current of the system is derived as

$$I_o = \frac{G_{U\_\text{inv}}G_{U\_\text{rec}}\sin^2(D\pi/2)\sin(\delta)V_i}{\omega M}. \tag{8}$$

For the conventional PSM method, both the inverter and rectifier operate in the FB mode, where G_{U_inv} and G_{U_rec} remain

fixed ($G_{U\_\mathrm{inv\_FB}} = G_{U\_\mathrm{rec\_FB}} = 2\sqrt{2}/\pi$). Within this configuration, the dc output current I_o is regulated by tuning the duty cycle D.

Moreover, to implement ZVS for the inverter and rectifier, the following relationship should be satisfied [23]:

$$\delta = D\pi/2 - \delta_m \tag{9}$$

where δ_m is the margin angle that ensures sufficient ZVS current for charging or discharging the equivalent output capacitance (C_{oss}) of the power switches.

C. Problems in MSCC Charging

As demonstrated by (8) and (9), achieving varying magnitudes of dc output current while implementing ZVS necessitates simultaneous adjustment of the duty cycle D and the phase angle δ. Nevertheless, at low charging currents, both D and δ should be reduced significantly to accommodate the required output. This reduction in D and δ leads to considerable reactive power in the resonant tank, which raises rms currents and decreases the transfer efficiency. Although the introduction of the HB mode ($G_{U\_\mathrm{inv\_HB}} = G_{U\_\mathrm{rec\_HB}} = \sqrt{2}/\pi$) can effectively reduce reactive power at lower current levels, the tuning range of this mode is still limited. During the trickle charging stage in MSCC applications, where the target charging current is notably low (e.g., 0.1 I_{o_rated}), significant reactive power persists even with the HB mode.

III. EHM-Based Dual-Side Control

As indicated by (8), if G_{U_inv} and G_{U_rec} can be adjusted in a broad range to accommodate the required output current (I_{o_set}), the reductions in D and δ can be minimized. This, in turn, contributes to decreased reactive power and improved efficiency. Therefore, this article introduces an EHM technique to broaden the tuning range of G_{U_inv} and G_{U_rec}. Based on the EHM technique, a dual-side control strategy, namely the EHM-DSC method, is further proposed. The following section elaborates on the proposed EHM technique and its associated control strategy.

A. Proposed EHM Technique

Fig. 6(a) demonstrates typical operating waveforms of the existing modes. As it can be observed from Fig. 6(a), when considering one switching cycle (T_s), there are four distinct operating modes: the FB mode, the HB mode, the reversed-half-bridge (RHB) mode, and the zero-voltage (ZV) mode. By distributing the above-mentioned modes in multiple switching cycles, hybrid modes with varying voltage gains (G_{U_inv} and G_{U_rec}) can be achieved. Fig. 6(b) further illustrates typical operating waveforms of the proposed hybrid modes, namely the HFR and HRZ modes. Specifically, the HFR mode distributes the HB, FB, and RHB modes evenly across three switching cycles, whereas the HRZ mode allocates the HB, RHB, and ZV modes. Moreover, the proposed HFR and HRZ modes exhibit the following characteristics.

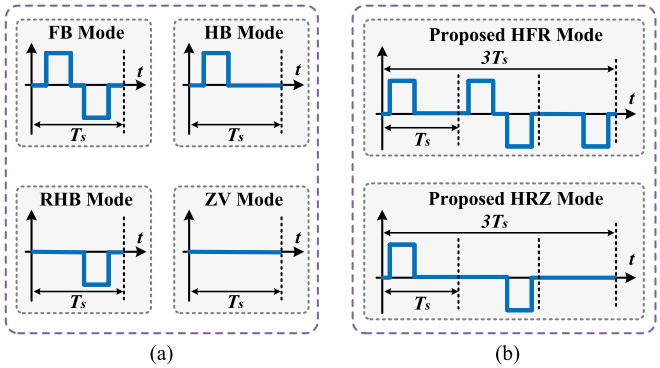

Fig. 6. Typical operating waveforms of (a) the existing modes considering one switching cycle (T_s), and (b) the proposed hybrid modes considering three switching cycles ($3T_s$). Notably, in the proposed EHM-DSC method, both the inverter and rectifier can operate in the specified HFR and HRZ modes.

1) Minimized subharmonics: As previously described, hybrid modes can be achieved by distributing FB, HB, RHB, and ZV modes across multiple switching cycles. Here, the number of selected switching cycles is denoted as N. Increasing N results in a greater variety of hybrid modes with a broader range of G_{U_inv} and G_{U_rec}. However, a larger N also introduces more subharmonics into the ac voltages (u_{ab} and u_{cd}), which in turn leads to increased distortion in the coil currents (i_P and i_S). Therefore, in the proposed HFR and HRZ modes, N is configured as 3 to obtain a satisfactory range of voltage gains while minimizing subharmonics. More importantly, within the proposed hybrid modes, voltage pulses are evenly and symmetrically distributed to eliminate even-subharmonics in u_{ab} and u_{cd}, thereby further decreasing subharmonics in these voltages.

According to the operating waveforms demonstrated in Fig. 6(b), the time-domain expressions for $u_{ab}(t)$ and $u_{cd}(t)$ under the proposed hybrid modes can be derived utilizing the Fourier series expansion

$$u_{ab}(t) = \sum_{n=\frac{1}{3},1,\frac{5}{3},\ldots} u_{ab,n}(t) = A_n \sin(n\omega t + \alpha_n) \tag{10}$$

$$u_{cd}(t) = \sum_{n=\frac{1}{3},1,\frac{5}{3},\ldots} u_{ab,n}(t) = B_n \sin(n\omega t + \beta_n). \tag{11}$$

Herein, A_n and α_n denote the amplitude and phase of subharmonics at the frequencies of $n\omega$ in u_{ab} ($n = 1/3, 1, 5/3, \ldots$), while B_n and β_n represent these parameters in u_{cd}. As evident from (10) and (11), the implementation of symmetrical pulse distributions eliminates even-subharmonics (subharmonics at the frequencies of $2\omega/3, 4\omega/3, \ldots$) in u_{ab} and u_{cd}, allowing only odd-subharmonics (subharmonics at the frequencies of $\omega/3, 5\omega/3, \ldots$) in these voltages.

2) Extended range of voltage gains: Fig. 7(a) demonstrates analytical operating waveforms for the proposed HRZ mode. As shown in Fig. 7(a), the HRZ mode can be regarded as a special case of the FB mode, with the switching cycle at $3T_s$. Therefore, when the inverter and rectifier operate in the HRZ mode, the time-domain expressions of $u_{ab,n}(t)$ and $u_{cd,n}(t)$ are

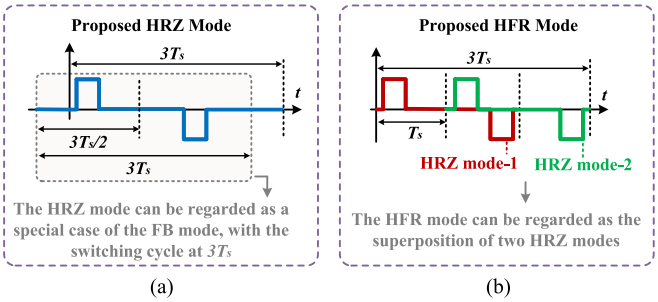

Fig. 7. Analytical operating waveforms of the proposed hybrid modes. (a) HRZ mode. (b) HFR mode.

derived as

$$u_{ab,n}(t) = \frac{4V_i}{3n\pi}\sin\left(\frac{3n\pi}{2}\right)\sin\left(\frac{nD\pi}{2}\right)\sin[n(\omega t+\pi)] \tag{12}$$

$$u_{cd,n}(t) = \frac{4V_o}{3n\pi}\sin\left(\frac{3n\pi}{2}\right)\sin\left(\frac{nD\pi}{2}\right)\sin[n(\omega t+\pi+\delta)]. \tag{13}$$

Moreover, substituting $n=1$ into (12) and (13), the fundamental components within $u_{ab}(t)$ and $u_{cd}(t)$ under the HRZ mode are formulated as

$$u_{ab,1}(t) = \frac{4V_i}{3\pi}\sin\left(\frac{D\pi}{2}\right)\sin(\omega t) \tag{14}$$

$$u_{cd,1}(t) = \frac{4V_o}{3\pi}\sin\left(\frac{D\pi}{2}\right)\sin(\omega t+\delta). \tag{15}$$

As indicated by (14) and (15), the corresponding voltage gains for the inverter and rectifier under the HRZ mode are

$$G_{U\_\text{inv\_HRZ}} = G_{U\_\text{rec\_HRZ}} = \frac{1}{3}\times\frac{2\sqrt{2}}{\pi}. \tag{16}$$

Regarding the HFR mode, as illustrated in Fig. 7(b), the voltage waveforms can be considered as the superposition of two HRZ modes, with one mode shifted by 2π relative to the other. Hence, when the inverter and rectifier work in the HFR mode, the time-domain expressions of $u_{ab,n}(t)$ and $u_{cd,n}(t)$ are

$$u_{ab,n}(t) = \frac{4V_i}{3n\pi}\sin\left(\frac{3n\pi}{2}\right)\sin\left(\frac{nD\pi}{2}\right)\{\sin[n(\omega t+\pi) + \sin[n(\omega t-\pi)]\} \tag{17}$$

$$u_{cd,n}(t) = \frac{4V_o}{3n\pi}\sin\left(\frac{3n\pi}{2}\right)\sin\left(\frac{nD\pi}{2}\right)\{\sin[n(\omega t+\pi+\delta)] + \sin[n(\omega t-\pi+\delta)]\}. \tag{18}$$

Furthermore, substituting $n=1$ into (17) and (18), the fundamental components within $u_{ab}(t)$ and $u_{cd}(t)$ under the HFR mode are derived as

$$u_{ab,1}(t) = \frac{8V_i}{3\pi}\sin\left(\frac{D\pi}{2}\right)\sin(\omega t) \tag{19}$$

$$u_{cd,1}(t) = \frac{8V_o}{3\pi}\sin\left(\frac{D\pi}{2}\right)\sin(\omega t+\delta). \tag{20}$$

TABLE I
MODE GAINS OF DIFFERENT OPERATING MODES

Operating mode	FB	HFR	HB	HRZ
Mode gains of the inverter and rectifier (G_{M_inv} and G_{M_rec})	1	$\frac{2}{3}$	$\frac{1}{2}$	$\frac{1}{3}$

Consequently, the corresponding voltage gains for the inverter and rectifier under the HFR mode are given by

$$G_{U\_\text{inv\_HFR}} = G_{U\_\text{rec\_HFR}} = \frac{2}{3}\times\frac{2\sqrt{2}}{\pi}. \tag{21}$$

As indicated by (16) and (21), the HRZ and HFR modes provide lower dc to ac voltage gains compared to the FB mode. The decreased voltage gains facilitate the implementation of lower charging currents in MSCC charging. Specifically, when the charging current falls below the rated level, the inverter and rectifier can transition from the FB mode to the HFR and HRZ modes, allowing for reduced output current without significantly decreasing the duty cycle of the inverter and rectifier.

B. Dual-Side Control Based on EHM

To effectively accommodate the varying magnitudes of dc output current, the proposed EHM-DSC method allows the inverter and rectifier to operate in four distinct modes: the FB, HFR, HB, and HRZ modes. For analytical convenience, the mode gains for the inverter (G_{M_inv}) and rectifier (G_{M_rec}) are defined as follows:

$$G_{M\_\text{inv}} = \frac{G_{U\_\text{inv}}}{2\sqrt{2}/\pi}, G_{M\_\text{rec}} = \frac{G_{U\_\text{rec}}}{2\sqrt{2}/\pi}. \tag{22}$$

Table I presents the mode gains for the inverter (G_{M_inv}) and rectifier (G_{M_rec}) across various operating modes. Furthermore, substituting (22) into (8) yields the expression for the dc output current under the proposed EHM-DSC method

$$I_o = \frac{8\sin^2(D\pi/2)\sin(\delta)V_i}{\pi^2\omega M}\times G_{M\_\text{sys}} \tag{23}$$

where

$$G_{M\_\text{sys}} = G_{M\_\text{inv}}G_{M\_\text{rec}}. \tag{24}$$

Herein, G_{M_sys} is defined as the overall mode gain of the system. As demonstrated by (23) and (24), through transitioning the inverter and rectifier modes, G_{M_sys} can be adjusted accordingly. Furthermore, by implementing strategic mode transitions across different MSCC stages, the regulation of the dc output current can be achieved.

Fig. 8 illustrates feasible operating modes of the system and their corresponding mode gains under the proposed EHM-DSC method. As indicated by Fig. 8, the proposed EHM-DSC method demonstrates two advantages compared with the existing FB-DSC and HM-DSC methods. First, the EHM-DSC method achieves a reduced minimum mode gain for the system. Specifically, the minimum system mode gain ($G_{M\_\text{sys\_min}}$) for the FB-DSC method is 1, while for the HM-DSC method, it is 1/4. In contrast, the EHM-DSC method reduces $G_{M\_\text{sys\_min}}$

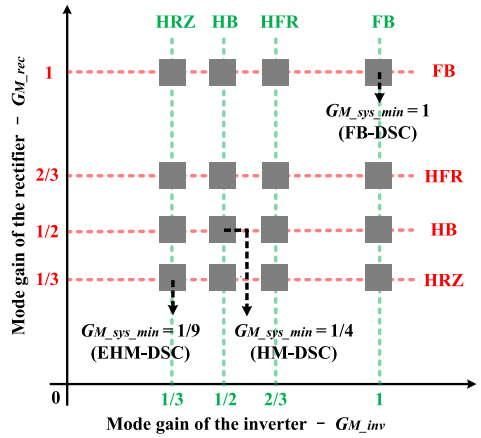

Fig. 8. Feasible operating modes of the system and their corresponding mode gains under the proposed EHM-DSC method. Herein, $G_{M\_\mathrm{sys\_min}}$ denotes the minimum mode gain of the system. Moreover, the FB-DSC and HM-DSC methods refer to the dual-side control methods based on the FB mode [19], [20] and the existing HM techniques [22], [23].

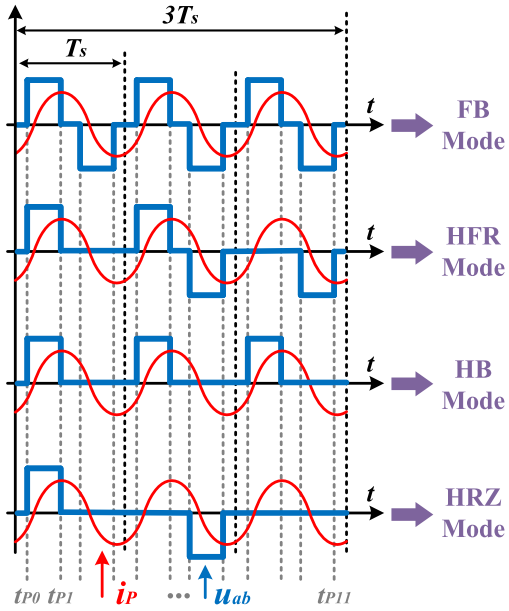

Fig. 9. Operating waveforms of u_{ab} and i_P when the inverter operates in the FB, HFR, HB, and HRZ modes. Herein, it is demonstrated that the coil current i_P lags the inverter output voltage u_{ab} for achieving the inverter ZVS.

to 1/9, offering a notable advantage during the trickle charging stage. Second, the EHM-DSC method provides a broader range of mode gains. By incorporating the HRZ and HFR modes, the EHM-DSC method supports up to 16 distinct operating modes for the system. This capability is especially advantageous for MSCC charging. Through transitioning between different modes, the dc output current can be regulated to various magnitudes without significantly adjusting the duty cycle D and the phase angle δ. This feature contributes to decreased reactive power across various MSCC stages, thereby enhancing the system's overall transmission efficiency.

C. Unified ZVS Model Considering Subharmonics

To investigate the optimal ZVS conditions for the proposed EHM-DSC approach, a unified ZVS model is developed to encompass all operating modes. In addition, subharmonics within the coil currents (i_P and i_S) are considered to derive the optimal ZVS conditions. Notably, due to the complexity of calculating multiple subharmonics, obtaining an explicit expression for the optimal ZVS conditions is difficult. However, this derivation process can be systematically achieved with a step-by-step procedure. The process for deriving the optimal ZVS conditions is detailed as follows.

1) *Identify the control variables:* The proposed EHM-DSC method defines four distinct control variables: the inverter mode, the rectifier mode, the duty cycle D, and the phase angle δ. Both the inverter and rectifier can operate at four modes: the HRZ, HB, HFR, and FB modes. In addition, the duty cycle D is constrained to [0, 1], while the phase angle δ is limited within [0°, 90°].
2) *Derive the Fourier expansions of $u_{ab}(t)$ and $u_{cd}(t)$:* According to the inverter and rectifier modes, along with the duty cycle D and phase angle δ, the Fourier expansions of $u_{ab}(t)$ and $u_{cd}(t)$ can be derived. Notably, the Fourier expansions of $u_{ab}(t)$ and $u_{cd}(t)$ for the FB and HB modes have been reported in [26] and [30], while those for the proposed HRZ and HFR modes are presented in Section III-A.
3) *Derive the time-domain expressions of $i_P(t)$ and $i_S(t)$:* Based on the Fourier expansions of $u_{ab}(t)$ and $u_{cd}(t)$, the time-domain expressions of $i_P(t)$ and $i_S(t)$ can be calculated. Specifically, applying KVL to the circuit topology depicted in Fig. 3, the phasor-domain expressions of $\dot{I}_{P,n}$ and $\dot{I}_{S,n}$ are derived as

$$\begin{bmatrix}\dot{I}_{P,n}\\ \dot{I}_{S,n}\end{bmatrix} = jH_n\begin{bmatrix}(n^2-1)L_S & n^2M\\ n^2M & (n^2-1)L_S\end{bmatrix}\begin{bmatrix}\dot{U}_{ab,n}\\ -\dot{U}_{cd,n}\end{bmatrix} \quad (25)$$

where

$$H_n = \frac{n}{\omega L_P L_S[(k^2-1)n^4+2n^2-1]}.$$

Furthermore, considering subharmonic components, the time-domain expressions for $i_P(t)$ and $i_S(t)$ are given by

$$i_P(t) = \sum_{n=\frac{1}{3},\frac{2}{3},1,\ldots} i_{P,n}(t), i_S(t) = \sum_{n=\frac{1}{3},\frac{2}{3},1,\ldots} i_{S,n}(t). \quad (26)$$

4) *Calculate the instantaneous values of $i_P(t)$ and $i_S(t)$ at the switching moments:* According to the time domain expressions of $i_P(t)$ and $i_S(t)$, the instantaneous values of $i_P(t)$ and $i_S(t)$ at the switching moments can be obtained. To define the switching moments for the inverter, Fig. 9 demonstrates the operating waveforms of u_{ab} and i_P when the inverter operates in the FB, HFR, HB, and HRZ modes. Notably, given that the maximum control cycle in the proposed hybrid modes is three switching cycles, it is

TABLE II
SPECIFICATIONS OF THE WPT SYSTEM

Symbol	Parameters	Value	Unit
L_P	Primary coil inductance	335.8	μH
L_S	Secondary coil inductance	220.0	μH
M	Mutual inductance	77.8	μH
C_P	Primary series capacitance	10.6	nF
C_S	Secondary series capacitance	16.1	nF
f_s	Resonant switching frequency	85	kHz
V_i	Dc input voltage	400	V
V_o	Dc output voltage	320–420	V
P_{o_rated}	Rated output power	3.0	kW

sufficient to consider only three switching cycles for the ZVS analysis. As shown in Fig. 9, to determine the ZVS conditions for the inverter, the instantaneous values of $i_P(t)$ at the switching moments $t_{P0}, t_{P1}, t_{P2}, \ldots, t_{P11}$ should be investigated. Specifically, define the switching moment of t_{P0} as

$$t_{P0} = \frac{(1-D)\pi}{2} \times \frac{T_s}{2\pi}. \tag{27}$$

As illustrated in Fig. 9, once t_{P0} is defined, the switching moments $t_{P1}, t_{P2}, \ldots, t_{P11}$ can be identified according to their phase relationships.

Moreover, the ZVS analysis for the rectifier is similar to that for the inverter. The primary difference is the presence of a phase difference angle δ between u_{ab} and u_{cd}. Taking this phase difference into account, the switching moment t_{S0} is indicated by

$$t_{S0} = t_{P0} - \delta \times \frac{T_s}{2\pi}. \tag{28}$$

Based on (28), the switching moments of $t_{S1}, t_{S2}, \ldots, t_{S11}$ can be determined as well.

Finally, substituting the switching moments t_{Pi} and t_{Sj} ($i = 1, 2 \ldots, 11$; $j = 1, 2, ..11$) into (26), the instantaneous values of $i_P(t)$ and $i_S(t)$ at the switching moments can be obtained.

5) *Identify the optimal ZVS conditions:* To ensure ZVS for all power switches, the unified ZVS condition is formulated as follows:

$$I_{\text{ZVS\_min}} \geq I_{\text{ZVS\_th}} \tag{29}$$

where $I_{\text{ZVS\_min}} = \min\{\min_i\{|i_P(t_{Pi})|\}, \min_j\{|i_S(t_{Sj})|\}\}$ is the minimum ZVS current, while $I_{\text{ZVS\_th}}$ is the threshold ZVS current to charge or discharge C_{oss}. Notably, given that all switching moments within three switching cycles are considered, the ZVS condition described by (29) can be applied to analyze ZVS across all hybrid modes, encompassing the FB, HFR, HB, and HRZ modes for both the inverter and rectifier.

Using the HRZ–HRZ mode (where both the inverter and rectifier operate in the HRZ mode) as an example and applying the system parameters from Table II, Fig. 10 presents the minimum ZVS current $I_{\text{ZVS\_min}}$ under various combinations of D and δ. As shown in Fig. 10, when the colorful surface is above the red plane, the ZVS condition described by (29) is satisfied. Moreover, the intersection line between the colorful surface and the red plane represents the optimal ZVS conditions, where the inverter and rectifier ZVS are achieved with minimal reactive power.

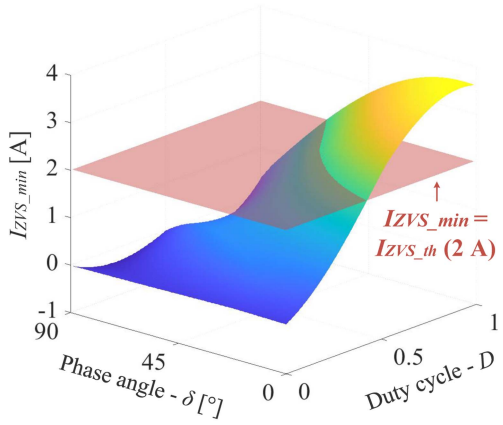

Fig. 10. Minimum ZVS current $I_{\text{ZVS\_min}}$ under various combinations of D and δ when both the inverter and rectifier operate in the HRZ mode. Herein, the threshold ZVS current $I_{\text{ZVS\_th}}$ is set as 2.0 A, while the required output current I_{o_set} is configured as 0.1 I_{o_rated}.

D. Overall Power Loss Analysis

The power losses of the system mainly encompass those incurred by the inverter, the resonant circuits, and the rectifier.

Specifically, the power losses of the inverter primarily arise from the conduction and switching losses of the MOSFETs. The conduction losses of the inverter are expressed as

$$P_{\text{inv\_con}} = 2R_{\text{on}}I_P^2 \tag{30}$$

where R_{on} is the conduction resistance of the MOSFETs. Moreover, the switching losses of the inverter are established as follows [22]:

$$P_{\text{inv\_sw}} = \sum_i |i_P(t_{Pi})|V_i \left(\frac{E_{\text{off}}}{V_R I_R} + \frac{Q_{RR}}{I_{RD}}\right)\frac{f_s}{3} \tag{31}$$

where E_{off} represents the turn-OFF energy losses of the MOSFET; V_R and I_R denote the reference drain-source voltage and source current of the MOSFET; Q_{RR} and I_{RD} are the reverse recovery charge and the reference current of the body diode; f_s is the switching frequency.

Similarly, the conduction and switching losses of the rectifier are formulated as

$$P_{\text{rec\_con}} = 2R_{\text{on}}I_S^2 \tag{32}$$

$$P_{\text{rec\_sw}} = \sum_j |i_S(t_{Sj})|V_o \left(\frac{E_{\text{off}}}{V_R I_R} + \frac{Q_{RR}}{I_{RD}}\right)\frac{f_s}{3}. \tag{33}$$

Furthermore, the power losses of the resonant circuits are given by

$$P_{\text{res}} = I_P^2 R_P + I_S^2 R_S \tag{34}$$

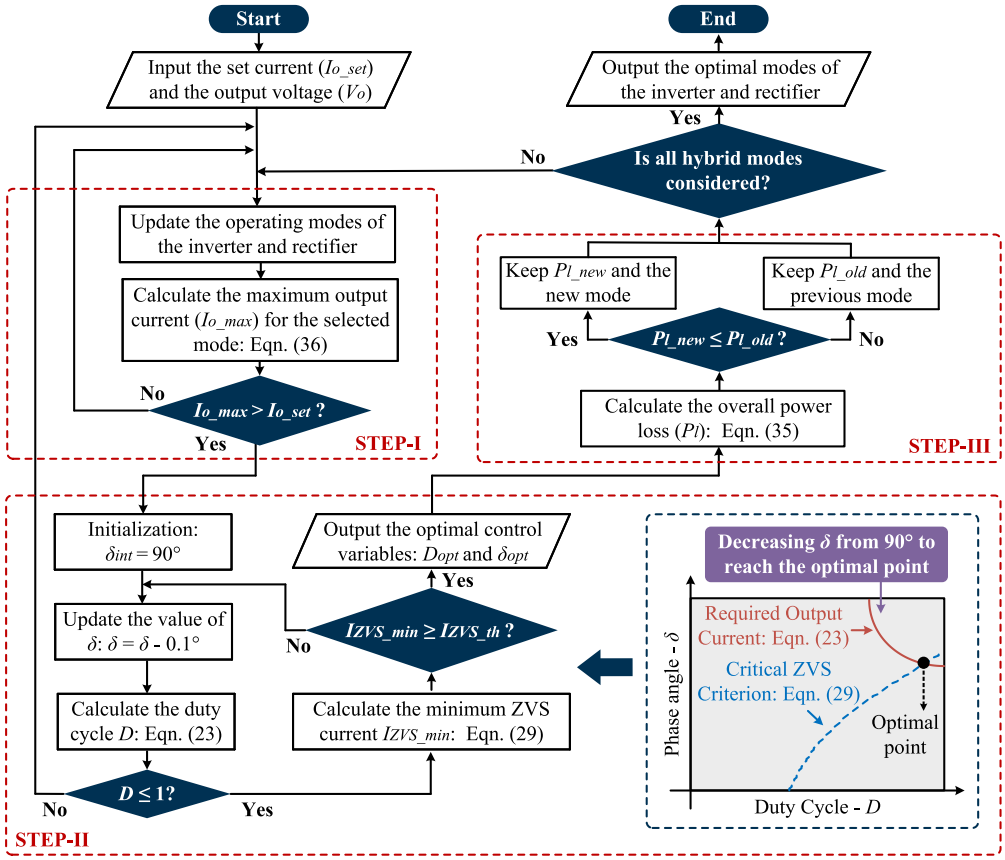

Fig. 11. Flowchart for identifying the optimal modes based on the MSCC charging profile.

where R_P and R_S are the equivalent loss resistances of the primary and secondary resonant circuits, respectively.

Consequently, the overall power loss of the system is obtained as

$$P_l = P_{\text{inv\_con}} + P_{\text{inv\_sw}} + P_{\text{rec\_con}} + P_{\text{rec\_sw}} + P_{\text{res}}. \quad (35)$$

E. Optimal Mode Trajectory for MSCC Charging

As previously analyzed in Fig. 8, the proposed EHM-DSC method provides up to 16 operating modes for the system. Therefore, it is important to identify the optimal modes for different MSCC stages. Fig. 11 demonstrates the flowchart for determining the optimal modes based on the required MSCC output. As illustrated in Fig. 11, the determination of optimal modes involves three steps. A detailed explanation of these steps is provided as follows.

Step-I. Determine whether the selected mode meets the output requirements: First, based on the MSCC profile, the target current (I_{o_set}) and the dc output voltage (V_o) are specified and utilized as the inputs. Subsequently, the available 16 operating modes are searched. Once the operating mode is identified, the maximum output current ($I_{o\_\max}$) of the selected mode can be obtained, as given by

$$I_{o\_\max} = \frac{8V_i G_{M\_\text{sys}}}{\pi^2 \omega M} \quad (36)$$

where G_{M_sys} is determined by the selected operating mode. If $I_{o\_\max}$ exceeds I_{o_set}, it indicates that the selected mode meets the output requirements and can proceed to step-II. Otherwise, another mode should be searched.

Step-II. Identify the optimal operating point under the selected mode: After the operating mode is determined, the optimal operating point, specifically, the optimal duty cycle (D_{opt}) and the optimal phase angle (δ_{opt}), should be identified. The determination of the optimal operating point is guided by two criteria. First, the optimal operating point needs to satisfy the required output current. According to the calculation of (23), the corresponding output current profile can be determined. Second, the optimal point should achieve both the inverter and rectifier ZVS with minimal reactive power. The optimal ZVS trajectory can be identified through the derivation of (29). Specifically, in the lower right corner of Fig. 11, an illustrative subfigure is provided to demonstrate how the optimal combination of δ_{opt} and D_{opt} is determined. Within this subfigure, when the combinations of δ and D are located on the red curve, the relationship described by (23) is satisfied, where the required output current I_{o_set} is obtained. On the other hand, if the combinations of δ and D lie on the blue curve, the relationship described by (29) is met, where the inverter and rectifier ZVS are achieved with minimal reactive power. The intersection point of the blue and red curves represents the optimal operating point.

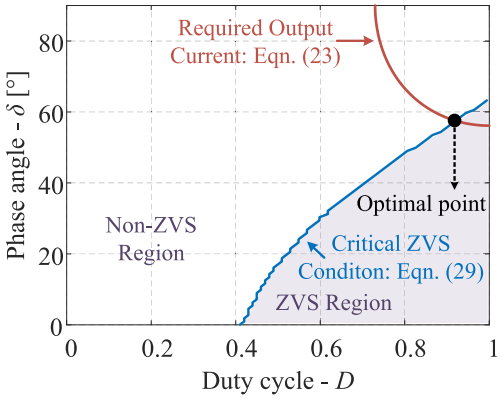

Fig. 12. Optimal ZVS trajectory and required output current profile when the inverter and rectifier both operate at the HRZ mode. Herein, the threshold ZVS current $I_{\mathrm{ZVS\_th}}$ is set as 2.0 A, while the required output current I_{o_set} is configured as 0.1 I_{o_rated}.

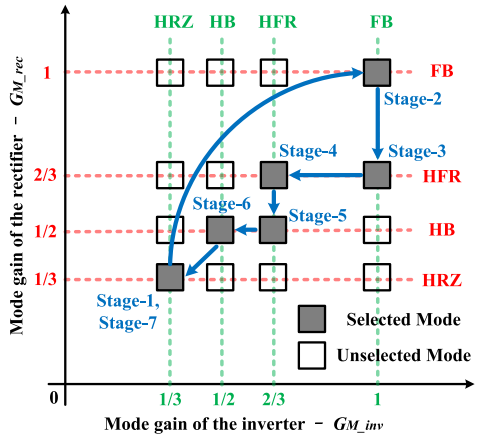

Fig. 13. Optimal mode trajectory for the seven-stage MSCC charging profile specified in Table III.

Here, a specific example is provided to illustrate the determination of the optimal operating point. Using the system parameters in Table II, Fig. 12 illustrates the required output current profile (the red curve) and the optimal ZVS trajectory (the blue curve) when delivering $0.1I_{o\_\mathrm{rated}}$ at the HRZ–HRZ mode. The required output current profile is derived by substituting the HRZ–HRZ mode gain and the required output current $0.1I_{o\_\mathrm{rated}}$ into (23). Moreover, the optimal ZVS trajectory is determined through the step-by-step derivation of (29). Notably, the optimal ZVS trajectory in Fig. 12 corresponds to the intersection line between the colorful surface and the red plane in Fig. 10. By projecting this intersection line onto the $D-\delta$ plane, the optimal ZVS trajectory in Fig. 12 is obtained accordingly. Furthermore, as illustrated in Fig. 12, the intersection point of the optimal ZVS trajectory and the required output current profile represents the optimal point for delivering the target current $0.1I_{o\_\mathrm{rated}}$. At this point, the desired output current is obtained while both the inverter and rectifier achieve ZVS with minimal reactive power.

Once the optimal point is identified, the flowchart proceeds to step-III.

Step-III. Select the optimal mode that minimizes overall power loss: In this step, the overall power loss of the system is calculated using (35). Subsequently, the obtained overall power loss is then compared with that of the previous mode. Finally, the operating mode that minimizes the overall power loss is selected and utilized as the output of this flowchart.

Utilizing the above-mentioned flowchart, the optimal mode trajectory can be derived based on the specified MSCC charging profile. Specifically, Fig. 13 illustrates the optimal mode trajectory for the seven-stage MSCC profile specified in Table III. As shown in Fig. 13, to handle the specified seven-stage profile, the proposed method begins in the HRZ–HRZ mode during stage-1, progresses to the FB–FB mode in stage-2, FB-HFR mode in stage-3, HFR–HFR mode in stage-4, HFR-HB mode in stage-5, HB–HB mode in stage-6, and finally returns to the HRZ–HRZ mode in stage-7. In addition to the seven-stage profile [13], the five-stage profile is also widely adopted [14], [29]. Fig. 14

TABLE III
SPECIFIED SEVEN-STAGE MSCC CHARGING PROFILE

No. of stage	Range of output voltage	Value of set current
1	320–336 V	0.72 A
2	337–420 V	7.20 A
3	408–420 V	4.32 A
4	410–420 V	2.88 A
5	412–420 V	2.16 A
6	414–420 V	1.44 A
7	416–420 V	0.72 A

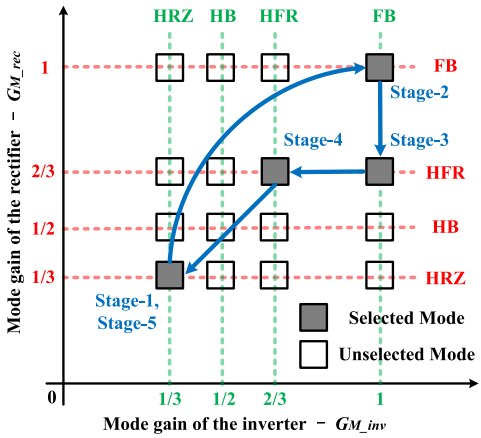

Fig. 14. Optimal mode trajectory for the five-stage MSCC charging profile specified in Table IV.

depicts the optimal mode trajectory for the five-stage profile detailed in Table IV. As shown in Fig. 14, when addressing the specified five-stage profile, the proposed method begins in the HRZ–HRZ mode during stage-1, progresses to the FB–FB mode in stage-2, FB-HFR mode in stage-3, HFR–HFR mode in stage-4, and finally returns to the HRZ-HR mode in stage-5.

It is noteworthy that while different MSCC profiles result in varying optimal mode trajectories, the methodology presented in this article is universal. By following the step-by-step process

TABLE IV
SPECIFIED FIVE-STAGE MSCC CHARGING PROFILE

No. of stage	Range of output voltage	Value of set current
1	320-336 V	0.72 A
2	337-420 V	7.20 A
3	408-420 V	4.20 A
4	412-420 V	2.80 A
5	416-420 V	0.72 A

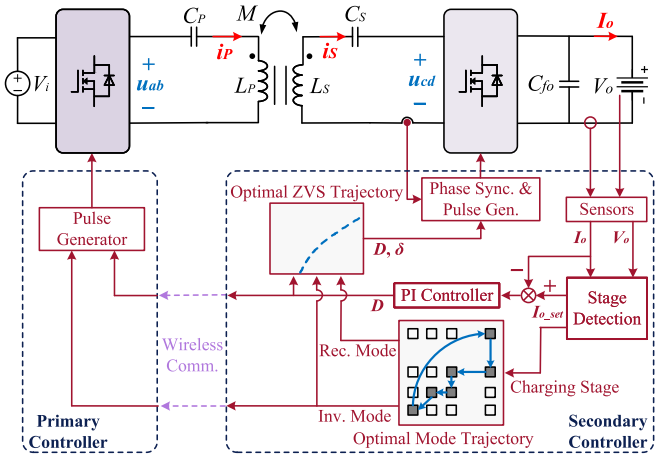

Fig. 15. Control block diagram of the proposed EHM-DSC method.

outlined in Fig. 11, the optimal mode trajectory can be derived for any specified MSCC profile.

F. Control Framework

The control block diagram of the proposed EHM-DSC method is demonstrated in Fig. 15. The implementation details of this approach are elaborated as follows.

First, the dc output voltage and current (V_o and I_o) are measured by the corresponding sensors. Based on the measured V_o and I_o, a stage detection module is utilized to determine the charging stage and the target current (I_{o_set}). For instance, Fig. 16 demonstrates the flowchart of stage detection for the seven-stage MSCC charging profile. As illustrated in Fig. 16, the pre-detection process identifies the initial charging stage based on the measured V_o. If V_o is less than V_{o_pre}, the charging process transitions to stage-1. Conversely, if V_o exceeds V_{o_pre}, the process shifts to stage-2. Furthermore, during the charging process, V_o is monitored in real-time. Based on this real-time measurement of V_o, the charging process transitions from stage-1 or stage-2 through to stage-7. Upon completion of the final stage (stage-7), the charging process is terminated.

Subsequently, based on the charging stage, the optimal inverter and rectifier modes are selected according to the optimal mode trajectory. On the other hand, a PI controller is implemented to ensure precise tracking of the reference target current (I_{o_set}). The PI controller determines the adjustment of the duty cycle D. Moreover, based on the optimal ZVS trajectory described by (29), the phase angle δ can be obtained accordingly.

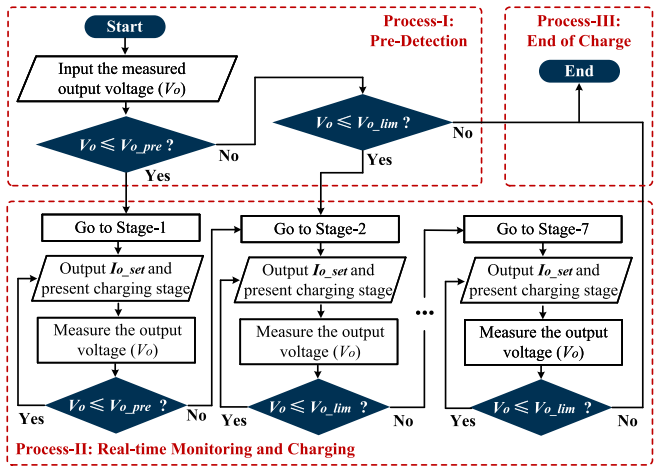

Fig. 16. Flowchart of stage detection for the seven-stage MSCC charging profile.

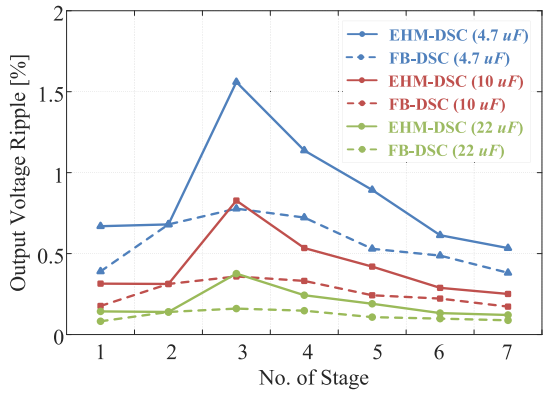

Fig. 17. Simulated dc output voltage ripple for various approaches with different dc output capacitances.

Finally, based on the obtained control variables (D and δ), as well as the optimal inverter and rectifier modes, the pulse generators are employed to produce the driving pulses for the inverter and rectifier.

Notably, the optimal modes and ZVS trajectories are pre-calculated and stored in the microcontroller in advance. During real-time operation, the microcontroller primarily handles the tasks of signal sensing, stage detection, PI control, and PWM generation. These tasks are well within the capabilities of commercially available microcontrollers.

G. Dc Output Voltage Ripple

To investigate the dc output voltage ripple of the proposed EHM-DSC method, Fig. 17 demonstrates the simulation results comparing the dc output voltage ripple across various approaches with different dc output capacitances. In these simulations, the dc output capacitance is varied for analysis, while the load is configured as a dc resistive load. As shown in Fig. 17, for the same dc output capacitance configurations, the proposed method results in a higher output voltage ripple compared to the conventional FB-DSC method. To achieve a comparable voltage

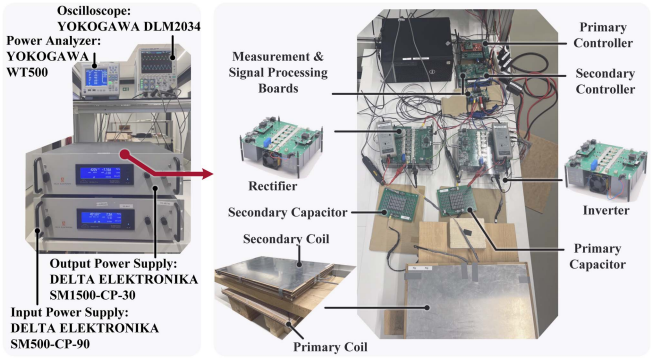

Fig. 18. Experimental platform.

ripple with the FB-DSC method, the proposed approach requires a larger dc output capacitance.

Nevertheless, it is worth emphasizing that, although the proposed method increases output voltage ripple, it demonstrates significant efficiency improvements over the FB-DSC method (see Fig. 26). In practical design, a tradeoff between efficiency improvements and increased output voltage ripple should be considered when evaluating the proposed method. Although applications with stringent requirements for output voltage ripple may necessitate a larger output capacitor to leverage the efficiency enhancement of the proposed method, it is important to note that for applications prioritizing energy transmission efficiency, the proposed method provides notable advantages.

IV. Experimental Results

A. Experimental Setup

To validate the effectiveness of the proposed EHM-DSC method for MSCC charging, a WPT prototype was developed, as shown in Fig. 18. The rated output power of this prototype was configured as 3.0 kW. The dc input voltage of the system was set at 400 V, which can be supplied by a frontend single-phase boost PFC converter in practice. The dc output voltage, on the other hand, was configured between 320 and 420 V to match the typical voltage range of a 400 V EV battery. Moreover, the seven-stage MSCC charging profile described in Table III was investigated. Within the experiments, the dc input and output voltages were provided by two bidirectional dc power supplies. In addition, two H-bridge converters were employed as the inverter and rectifier, with the operating frequency of these converters fixed at 85 kHz. The control algorithm and pulse generation were implemented utilizing TI Launchpads F28379D. Further electrical parameters of the developed prototype are demonstrated in Table II.

Notably, within the system, the contactless coils generate high-frequency magnetic fields for energy transmission. Meanwhile, signal processing circuits are crucial for modulation and control. Hence, it is important to address potential interference between the high-frequency electromagnetic fields and signal processing circuits. To mitigate electromagnetic interference, the following measures are implemented.

1) *Physical separation:* The main power circuits and signal processing circuits are positioned separately. By placing the signal processing circuits at a distance from the coils, the interference is significantly attenuated.
2) *Signal transmission techniques:* To reduce electromagnetic interference, PWM signals are transmitted via optical fibers. In addition, Ethernet cables are employed for transmitting analog voltage and current signals.
3) *Magnetic shielding:* Aluminum shielding is applied to the coils to attenuate stray magnetic fields. It is important to highlight that the primary focus of the proposed method is to enhance transmission efficiency and facilitate MSCC charging using advanced modulation and control techniques. In practical applications, the spatial arrangements and magnetic shielding design can be further optimized to minimize electromagnetic interference while improving system compactness.

B. Operating Waveforms and Output Performances

Fig. 19 illustrates key operating waveforms of the proposed EHM-DSC method for the MSCC profile specified in Table III. The proposed approach enables mode transitions according to the optimal mode trajectory described in Fig. 13. Through enabling these mode transitions, the proposed method facilitates varying output currents in various charging stages. Furthermore, by adjusting the duty cycle D of the inverter and rectifier ac voltages, the proposed approach offers precise current regulation capability to satisfy specific charging current demands. In addition, by regulating the phase angle δ, ZVS is achieved for both the inverter and rectifier across all charging stages. As illustrated in Fig. 19, the proposed mode transition strategy allows the duty cycle D to remain consistently high while maintaining a large phase angle δ for achieving ZVS. This, in turn, minimizes circulating reactive power within the resonant circuits, leading to reduced rms currents and enhanced efficiency.

Fig. 20 demonstrates the FFT analysis of the coil currents for the experimental results depicted in Fig. 19. As shown in Fig. 20, through symmetrically distributing the voltage pulses, the proposed HRZ and HFR modes eliminate even-subharmonics (subharmonics at the frequencies of $2\omega/3$, $4\omega/3$,.. .) in the coil currents. Moreover, due to the bandpass filtering characteristic of the SS compensation, the odd subharmonics (subharmonics at the frequencies of $\omega/3$, $5\omega/3$,.. .) in the coil currents are significantly mitigated. Consequently, the coil currents primarily remain at the fundamental frequency of ω. Although subharmonics in the coil currents are significantly smaller than the fundamental component, it is still important to examine their impacts. First, the presence of subharmonics in the coil currents can influence the system's output power, subsequently affecting the dc output current. However, in the proposed method, the closed-loop control (PI control) effectively guarantees accurate output tracking. Secondly, the subharmonics can influence the instantaneous values of the coil currents at the switching moments, affecting the implementation of ZVS. To address this, Section III-C demonstrates a step-by-step procedure for deriving the optimal ZVS conditions while accounting for subharmonic

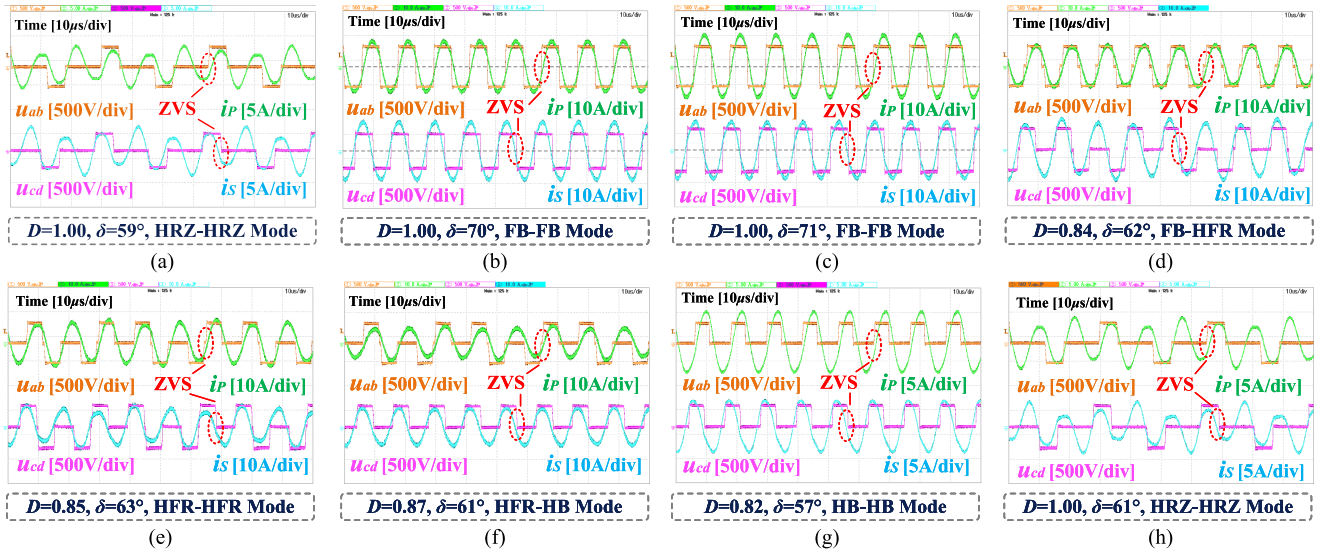

Fig. 19. Key operating waveforms of the proposed EHM-DSC method in different MSCC stages. (a) Stage-1 ($V_o = 336$ V, $I_o = 0.72$ A). (b) Stage-2 ($V_o = 337$ V, $I_o = 7.20$ A). (c) Stage-2 ($V_o = 420$ V, $I_o = 7.20$ A). (d) Stage-3 ($V_o = 420$ V, $I_o = 4.32$ A). (e) Stage-4 ($V_o = 420$ V, $I_o = 2.88$ A). (f) Stage-5 ($V_o = 420$ V, $I_o = 2.16$ A). (g) Stage-6 ($V_o = 420$ V, $I_o = 1.44$ A). (h) Stage-7 ($V_o = 420$ V, $I_o = 0.72$ A).

components. By incorporating these components into the analysis, the optimal ZVS conditions for both the inverter and rectifier are established, enabling optimal ZVS operation with minimal reactive power.

Fig. 21 shows the measured dc output voltages and charging currents in distinct MSCC stages. As illustrated in Fig. 21, the proposed method effectively achieves the required charging currents. Furthermore, Fig. 22 presents the measured output power and dc-to-dc efficiency at different stages. As evident from Fig. 22, the maximum output power of the system is 3.015 kW, measured at the endpoint of stage-2, while the minimum output power is 231 W, measured at the beginning point of stage-1. Although the proposed method accommodates a significantly wide power range from 231 W to 3.015 kW, the system maintains high efficiency throughout all charging stages, with a peak dc-to-dc efficiency of 95.67% and a minimum dc-to-dc efficiency of 92.45%.

It is important to note that the measured dc-to-dc efficiency accounts only for the power losses in the main power conversion circuits. The auxiliary circuits, such as digital signal processors and sensors, are powered by external dc adapters, and the power losses from these circuits are not measured.

C. Efficiency Comparisons and Power Loss Analysis

To highlight the advantages of the proposed EHM-DSC method, Fig. 23 provides a comparative analysis of the proposed EHM-DSC method against existing approaches, focusing on system performance at stage-1 ($V_o = 320$ V, $I_o = 0.72$ A). At this stage, the charging current is significantly low, approximately $0.1I_R$. To achieve such a low current, the conventional FB-DSC method still operates in FB–FB mode, while the existing HM-DSC method utilizes HB–HB mode. In contrast, the proposed EHM-DSC method employs HRZ–HRZ mode. Compared to the conventional FB-DSC and existing HM-DSC methods, the proposed approach demonstrates the following advantages.

1) *Decreased rms currents:* As shown in Fig. 23, the introduction of the HRZ–HRZ mode enables a higher duty cycle D and phase angle δ compared to the HB–HB and FB–FB modes. When delivering the same amount of output power (around 231 W), the proposed EHM-DSC method increases the value of δ from 18° (FB-DSC) and 38° (HM-DSC) to 59°. As described in Section II-A, a larger phase angle δ contributes to reduced reactive power circulating within the resonant circuits. Fig. 24 further demonstrates a quantitative analysis of circulating reactive power based on experimental results from Fig. 23. As shown in Fig. 24, by increasing the value of δ, the proposed EHM-DSC method reduces the reactive power from 714.3 Var (FB-DSC) and 296.6 Var (HM-DSC) to 138.9 Var. The decreased reactive power results in lower rms currents. In comparison with the conventional FB–FB mode, the proposed HRZ–HRZ mode reduces the primary rms current from 4.1 to 2.6 A and the secondary rms current from 4.2 to 3.0A. Similarly, compared to the existing HB–HB mode, the HRZ–HRZ mode lowers the primary rms current from 3.2 to 2.6 A and the secondary rms current from 3.5 to 3.0 A. This reduction in rms currents decreases conduction losses in the converters, coils, and capacitors.
2) *Reduced turn-OFF currents:* Further observation of Fig. 23 reveals that the proposed method achieves significantly lower turn-OFF currents due to higher duty cycle D and phase angle δ . Specifically, compared to the conventional FB–FB mode, the proposed HRZ–HRZ mode reduces the inverter turn-OFF current from 5.1 to 1.9 A and the rectifier turn-OFF current from 5.2 to 2.0 A. Similarly, compared to the existing HB–HB mode, the HRZ–HRZ mode decreases the inverter turn-OFFcurrent from 4.9 to 1.9 A and

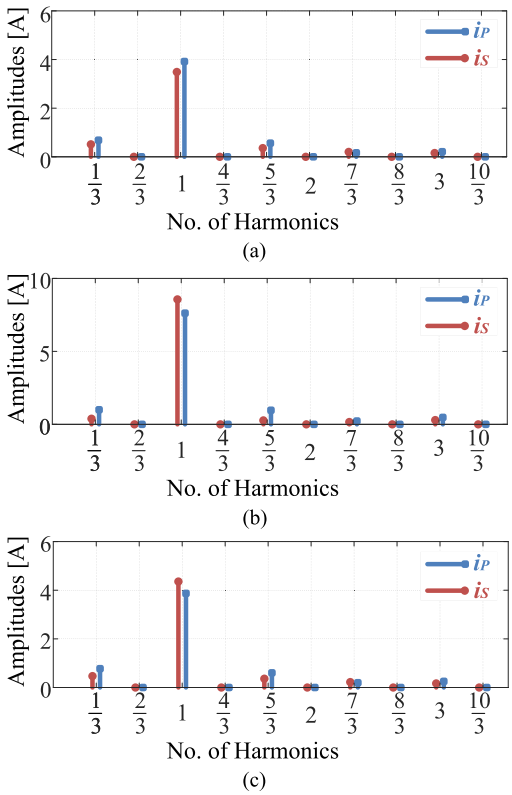

Fig. 20. FFT analysis of the coil currents (i_P and i_S) for the experimental results depicted in Fig. 19. (a) Stage-1 (HRZ–HRZ mode, $V_o = 336$ V, $I_o = 0.72$ A). (b) Stage-4 (HFR–HFR mode, $V_o = 420$ V, $I_o = 2.88$ A). (c) Stage-7 (HRZ–HRZ mode, $V_o = 420$ V, $I_o = 0.72$ A).

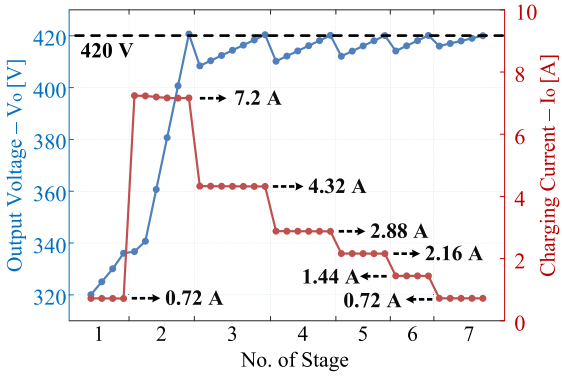

Fig. 21. Measured dc output voltages and charging currents in different MSCC stages using the proposed EHM-DSC method.

the rectifier turn-OFF current from 5.2 to 2.0 A. These reductions in turn-OFFcurrents contribute to significantly lower switching losses in the converters.

3) *Minimized switching events:* The proposed HRZ–HRZ mode significantly reduces switching events for both the inverter and rectifier. As shown in Fig. 23, when the inverter operates in the HRZ mode, it experiences only four switching events over three switching cycles ($3T_s$), compared to six events in the HB mode and 12 events in the FB mode. Considering both the inverter and rectifier, the proposed method decreases the total number of switching events from 24 events (FB–FB mode) and 12 events (HB–HB mode) to only eight events (HRZ–HRZ mode) over three switching cycles. This reduction in switching events leads to notably lower switching losses in the converters.

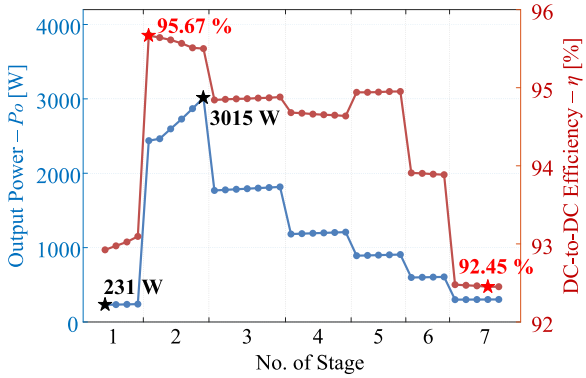

Fig. 22. Measured output power and dc-to-dc efficiency in different MSCC stages using the proposed EHM-DSC method.

Furthermore, Fig. 25 illustrates the power loss breakdown for the experimental results presented in Fig. 23. As shown in Fig. 25, by providing decreased rms currents, reduced turn-OFF currents, and minimized switching events, the proposed method achieves significant loss reductions in each part of the system. Consequently, when the charging system operates at stage-1 ($V_o = 320$V, $I_o = 0.72$ A), the proposed method enhances efficiency from 83.44% (FB–FB mode) and 90.16% (HB–HB mode) to 92.93% (HRZ–HRZ mode).

Fig. 26 presents efficiency comparisons throughout the entire MSCC charging process. As demonstrated in Fig. 26, the proposed EHM-DSC method significantly improves overall efficiency throughout the charging process, achieving a maximum efficiency improvement of up to 2.86% when compared with the existing HM-DSC method. Notably, during the MSCC charging, the system's output power (see the gray dotted line in Fig. 26) exhibits significant variations across different charging stages, which in turn leads to notable changes in the measured efficiencies.

D. Dynamic Performance

To validate the dynamic performance of the proposed EHM-DSC approach, the experimental prototype was tested under stage transitions and voltage variations. In the experiments, the dc output voltage and current were measured and processed by a measurement and signal processing board, while a PI controller was implemented in the TI launchpads to achieve the reference tracking.

Fig. 27 demonstrates the dynamic performance of the proposed method. As shown in Fig. 27(a), when the charging stage transitions from stage-1 to stage-2, the system's operating mode switches from the HRZ–HRZ mode to the FB–FB mode, while the dc output current is adjusted from 0.72 to 7.2 A. The proposed method effectively tracks the reference current in approximately 1.2 s. In addition, Fig. 27(b) illustrates the dynamic performance

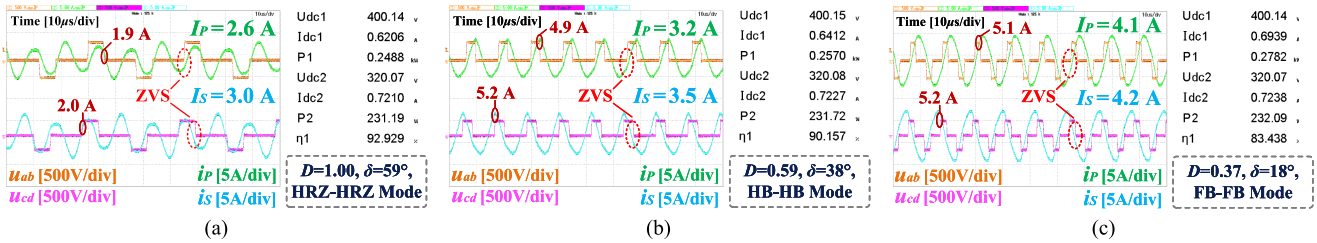

Fig. 23. Measured operating waveforms and dc-to-dc efficiency for various approaches at stage-1 ($V_o = 320$ V, $I_o = 0.72$ A). (a) Proposed EHM-DSC method. (b) Existing HM-DSC method. (c) Conventional FB-DSC method. Within this figure, Udc1, Idc1, and $P1$ represent the dc input voltage, current and power; Udc2, Idc2, and $P2$ denote the dc output voltage, current, and power; $\eta 1$ ($\eta 1 = P2/P1$) demonstrates the dc-to-dc efficiency.

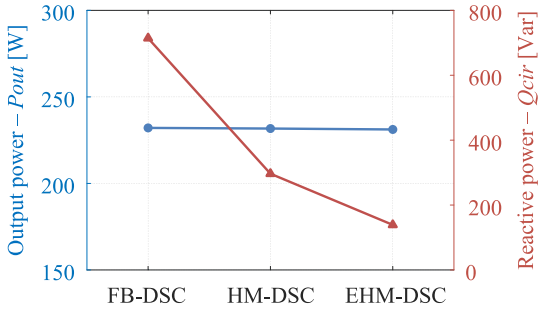

Fig. 24. Quantitative analysis of circulating reactive power based on experimental results from Fig. 23.

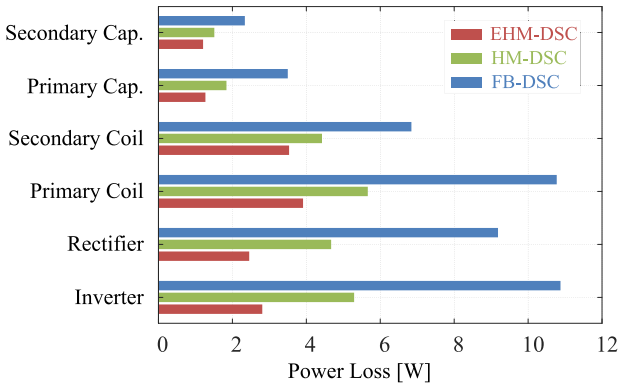

Fig. 25. Power loss analysis for the experimental results shown in Fig. 23.

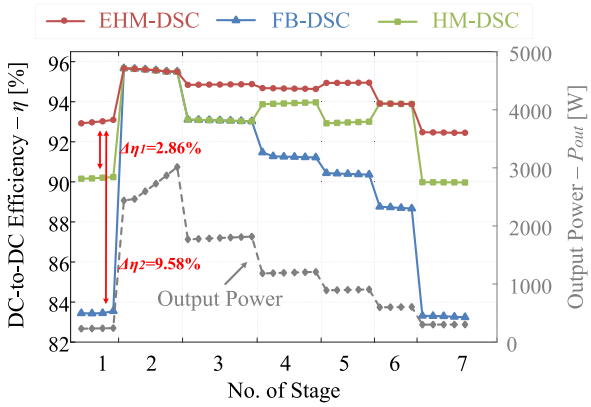

Fig. 26. Efficiency comparisons over the entire MSCC charging process. Here, the colorful solid lines show the measured dc-to-dc efficiencies of various approaches, while the gray dotted line indicates the system's output power.

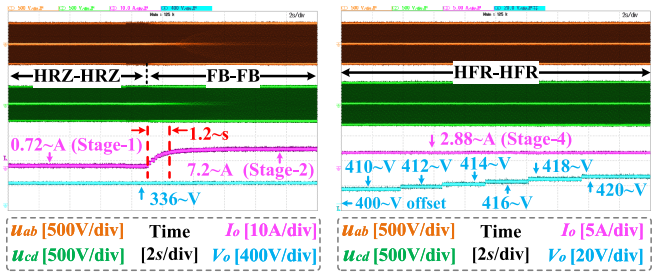

Fig. 27. Dynamic performance of the proposed EHM-DSC method. (a) When the charging stage transitions from stage-1 to stage-2. (b) When the output voltage varies from 410 to 420 V within stage-4.

within the same stage. When the output voltage varies from 410 to 420 V within stage-4, the proposed method maintains a constant output current of 2.88 A, demonstrating its ability to achieve CC output for MSCC charging.

V. Conclusions and Future Work

This article proposes an EHM-DSC approach to enable high transmission efficiency in wireless MSCC charging of EVs. By introducing two novel operating modes, i.e., the HRZ and HFR modes, the proposed EHM technique broadens the modulation range of the conventional PSM. Applying the EHM method to both the inverter and active rectifier further extends the output tuning capability of the system, facilitating wide-range MSCC outputs. Moreover, the implementation of optimal mode trajectory ensures ZVS for all power switches while minimizing the overall power loss of the system. Experimental results confirm that the proposed EHM-DSC approach successfully achieves MSCC charging and demonstrates a notable efficiency improvement of up to 2.86% compared to the existing HM-DSC method.

It is worth noting that this article investigates the most widely used SS compensation topology. However, other compensation structures, such as LCC-S and LCC–LCC, are gaining more and more popularity. Unlike the SS topology, the harmonic components within the inductor currents are not significantly

mitigated in LCC-S and LCC–LCC topologies. Therefore, when applying the proposed EHM-DSC method to these topologies, the harmonic components in the coil currents should be further investigated. The research on how to extend the proposed approach to these topologies is regarded as future work.

REFERENCES

[1] V. Z. Barsari, D. J. Thrimawithana, S. Kim, and G. A. Covic, "Modular coupler with integrated planar transformer for wireless EV charging," *IEEE Trans. Power Electron.*, vol. 38, no. 7, pp. 9206–9217, Jul. 2023.

[2] V.-B. Vu, D.-H. Tran, and W. Choi, "Implementation of the constant current and constant voltage charge of inductive power transfer systems with the double-sided LCC compensation topology for electric vehicle battery charge applications," *IEEE Trans. Power Electron.*, vol. 33, no. 9, pp. 7398–7410, Sep. 2018.

[3] X. Qu, H. Chu, S.-C. Wong, and K. T. Chi, "An IPT battery charger with near unity power factor and load-independent constant output combating design constraints of input voltage and transformer parameters," *IEEE Trans. Power Electron.*, vol. 34, no. 8, pp. 7719–7727, Aug. 2019.

[4] L. Yang, X. Li, S. Liu, Z. Xu, and C. Cai, "Analysis and design of an LCCC/s-compensated WPT system with constant output characteristics for battery charging applications," *IEEE Trans. Emerg. Sel. Topics Power Electron.*, vol. 9, no. 1, pp. 1169–1180, Feb. 2021.

[5] *The Wireless Power Transfer for Light-Duty Plug-in/Electric Vehicles and Alignment Methodology*, Standard SAE J2954. [Online]. Available: www.sae.org/standards/content/j2954_202010/

[6] W. Xiong, Z. Yan, D. Tang, W. Zhou, and R. Mai, "A hybrid topology IPT system with partial power processing for CC-CV charging," *IEEE Trans. Power Electron.*, vol. 39, no. 1, pp. 1701–1712, Jan. 2024.

[7] D. Wang, E. Zhang, C. Fu, X. Bei, and Q. Zhao, "A dynamic reconfiguration based hybrid network design methodology for IPT CC/CV output," *IEEE J. Emerg. Sel. Top. Power Electron.*, vol. 12, no. 1, pp. 367–377, Feb. 2024.

[8] Y. Zhang, Z. Shen, W. Pan, H. Wang, Y. Wu, and X. Mao, "Constant current and constant voltage charging of wireless power transfer system based on three-coil structure," *IEEE Trans. Ind. Electron.*, vol. 70, no. 1, pp. 1066–1070, Jan. 2023.

[9] X. Hu, Y. Zheng, X. Lin, and Y. Xie, "Optimal multistage charging of NCA/graphite lithium-ion batteries based on electrothermal-aging dynamics," *IEEE Trans. Transport. Electrific.*, vol. 6, no. 2, pp. 427–438, Jun. 2020.

[10] A. B. Khan and W. Choi, "Optimal charge pattern for the high-performance multistage constant current charge method for the Li-ion batteries," *IEEE Trans. Energy Convers.*, vol. 33, no. 3, pp. 1132–1140, Sep. 2018.

[11] C. Chen, Z. Wei, and A. C. Knoll, "Charging optimization for li-ion battery in electric vehicles: A review," *IEEE Trans. Transport. Electrific.*, vol. 8, no. 3, pp. 3068–3089, Sep. 2022.

[12] Z. Zhao et al., "Power electronics-based safety enhancement technologies for lithium-ion batteries: An overview from battery management perspective," *IEEE Trans. Power Electron.*, vol. 38, no. 7, pp. 8922–8955, Jul. 2023.

[13] J. Liu, C. S. Wong, C. Sun, F. Xu, X. Jiang, and K. Loo, "Software-reconfigurable multistage constant current wireless battery charging based on multiharmonic power transmission," *IEEE Trans. Power Electron.*, vol. 38, no. 4, pp. 5586–5597, Apr. 2023.

[14] Y. Xu, Y. Li, Y. Chen, W. Zhou, R. Mai, and Z. He, "A multiple-gain-reconfigurable-rectifier-based IPT system for battery multistage constant current high-efficiency wireless charging," *IEEE Trans. Power Electron.*, vol. 39, no. 1, pp. 1853–1869, Jan. 2024.

[15] L. Xue et al., "Design and analysis of a 200 kw dynamic wireless charging system for electric vehicles," in *Proc. 2022 IEEE Appl. Power Electron. Conf. Expo.*, IEEE, 2022, pp. 1096–1103.

[16] Z. Zhou, L. Zhang, Z. Liu, Q. Chen, R. Long, and H. Su, "Model predictive control for the receiving-side DC–DC converter of dynamic wireless power transfer," *IEEE Trans. Power Electron.*, vol. 35, no. 9, pp. 8985–8997, Sep. 2020.

[17] M. Li, J. Deng, D. Chen, W. Wang, Y. Li, and Z. Wang, "A minimum ZVS current control strategy of semi bridgeless active rectifier for wide operation range based on LCC-S compensated WPT system," *IEEE Trans. Ind. Appl.*, vol. 59, no. 3, pp. 3481–3492, May/Jun. 2023.

[18] G. Zhu, J. Dong, T. B. Soeiro, H. Vahedi, and P. Bauer, "Dual-side capacitor tuning and cooperative control for efficiency-optimized wide output voltages in wireless EV charging," *IEEE Trans. Ind. Electron.*, vol. 72, no. 3, pp. 2507–2518, Mar. 2025.

[19] G. Zhu, J. Dong, F. Grazian, and P. Bauer, "A hybrid modulation scheme for efficiency optimization and ripple reduction in secondary side controlled wireless power transfer systems," *IEEE Trans. Transport. Electrific.*, early access, Dec., 16, 2024, doi: 10.1109/TTE.2024.3517701.

[20] X. Zhang et al., "A control strategy for efficiency optimization and wide ZVS operation range in bidirectional inductive power transfer system," *IEEE Trans. Ind. Electron.*, vol. 66, no. 8, pp. 5958–5969, Aug. 2019.

[21] S. Chen et al., "An operation mode selection method of dual-side bridge converters for efficiency optimization in inductive power transfer," *IEEE Trans. Power Electron.*, vol. 35, no. 10, pp. 9992–9997, Oct. 2020.

[22] Y. Li, W. Sun, X. Zhu, and J. Hu, "A hybrid modulation control for wireless power transfer systems to improve efficiency under light-load conditions," *IEEE Trans. Ind. Electron.*, vol. 69, no. 7, pp. 6870–6880, Jul. 2022.

[23] G. Zhu, J. Dong, W. Shi, T. B. Soeiro, J. Xu, and P. Bauer, "A mode-switching-based phase shift control for optimized efficiency and wide ZVS operations in wireless power transfer systems," *IEEE Trans. Power Electron.*, vol. 38, no. 4, pp. 5561–5575, Apr. 2023.

[24] Y. Xu, Z. Yu, J. Chen, and Y. Wang, "A variable frequency phase-shift modulation constant power control strategy for LCC resonant capacitor charging power supply," *IEEE Trans. Ind. Electron.*, vol. 70, no. 2, pp. 1883–1893, Feb. 2023.

[25] A. Mostafa et al., "Output power regulation of a series-series inductive power transfer system based on hybrid voltage and frequency tuning method for electric vehicle charging," *IEEE Trans. Ind. Electron.*, vol. 69, no. 10, pp. 9927–9937, Oct. 2022.

[26] G. Zhu, J. Dong, G. Yu, W. Shi, C. Riekerk, and P. Bauer, "Optimal multivariable control for wide output regulation and full-range efficiency optimization in LCC-LCC compensated wireless power transfer systems," *IEEE Trans. Power Electron.*, vol. 39, no. 9, pp. 11834–11848, Sep., 2024.

[27] X. Zhang, R. Xue, F. Wang, F. Xu, T. Chen, and Z. Chen, "Capacitor tuning of LCC-LCC compensated IPT system with constant-power output and large misalignments tolerance for electric vehicles," *IEEE Trans. Power Electron.*, vol. 38, no. 10, pp. 11928–11939, Oct. 2023.

[28] G. Zhu, J. Dong, F. Grazian, and P. Bauer, "A parameter recognition based impedance tuning method for SS-compensated wireless power transfer systems," *IEEE Trans. Power Electron.*, vol. 38, no. 11, pp. 13298–13314, Nov. 2023.

[29] I.-W. Iam, Z. Ding, C.-F. Ieong, C.-S. Lam, R. P. Martins, and P.-I. Mak, "Optimal bivariate control strategy of multi-stage constant current charging for IPT-based wireless electric vehicle charging," *IEEE Trans. Transport. Electrific.*, vol. 10, no. 2, pp. 4513–4528, Jun. 2024.

[30] N. Fu, J. Deng, Z. Wang, W. Wang, and S. Wang, "A hybrid mode control strategy for LCC–LCC-compensated WPT system with wide ZVS operation," *IEEE Trans. Power Electron.*, vol. 37, no. 2, pp. 2449–2460, Feb. 2022.

Gangwei Zhu (Graduate Student Member, IEEE) received the B.S. degree from Central South University, Changsha, China, in 2018, the M.S. degree from Shanghai Jiao Tong University, Shanghai, China, in 2021, and the Ph.D. degree from Delft University of Technology, Delft, The Netherlands, in 2024, all in electrical engineering.

His research interests include design, modeling, and control for power electronics and wireless power transfer.

Shibo Zhang (Graduate Student Member, IEEE) received the B.S. degree from the Huazhong University of Science and Technology, Wuhan, China, in 2020, and the M.S. degree from Shanghai Jiao Tong University, Shanghai, China, in 2023, both in electrical engineering. He is currently working toward the Ph.D. degree in electrical engineering with the Delft University of Technology, Delft, The Netherlands.

His research interests include the design, modeling, and optimization of wireless power transfer systems.

Zichen Deng (Graduate Student Member, IEEE) received the B.S. and M.Sc. degrees in electrical engineering from Xi'an Jiaotong University, Xi'an, China, in 2020 and 2023, respectively. He is currently working toward the Ph.D. degree in wireless charging of electric vehicles with DC System, Energy Conversion and Storage (DCE&S) Group, Delft University of Technology, Delft, The Netherlands.

His research interests include wireless power transfer and pulsed power technology.

Jundong Wang (Graduate Student Member, IEEE) was born in Hefei, China, in 1998. He received the B.S. and M.S. degrees in electrical engineering from Southeast University, Nanjing, China, in 2020 and 2023, respectively. He is currently working toward the Ph.D. degree in electrical engineering with the Delft University of Technology, Delft, The Netherlands.

His research interests include modeling and control of electric propulsion system for aircraft.

Yongpeng Li (Graduate Student Member, IEEE) received the B.S. degree in electrical engineering and automation from Shanghai University, Shanghai, China, in 2019, and the M.S. degree in electrical and electronic engineering from the University of Sheffield, Sheffield, U.K., in 2020. He is currently working toward the Ph.D. degree in electrical engineering with DC System, Energy Conversion and Storage (DCE&S) Group, Delft University of Technology, Delft, The Netherlands.

His research interests include design of power inverter and the position sensorless drive for PMSM.

Jianning Dong (Senior Member, IEEE) received the B.S. and Ph.D. degrees in electrical engineering from Southeast University, Nanjing, China, in 2010 and 2015, respectively.

He was a Postdoctoral Researcher with the McMaster Automotive Resource Centre, McMaster University, Hamilton, ON, Canada. Since 2016, he has been an Assistant Professor with DC System, Energy Conversion and Storage (DCE&S) Group, Delft University of Technology, Delft, The Netherlands. His research interests include electromechanical energy conversion and contactless power transfer.

Pavol Bauer (Senior Member, IEEE) received the master's degree from the Technical University of Kosice, Kosice, Slovakia, in 1985, and the Ph.D. degree from the Delft University of Technology, Delft, The Netherlands, in 1995, both in electrical engineering.

From 2002 to 2003, he was with KEMA (DNV GL), Arnhem, The Netherlands, on different projects related to power electronics applications in power systems. He is currently a Full Professor with the Department of Electrical Sustainable Energy, Delft University of Technology, and the Head of DC Systems, Energy Conversion, and Storage Group. He is also a Professor with the Brno University of Technology, Brno, Czech Republic, and an Honorary Professor with the Politehnica University Timisoara, Timisoara, Romania. He has authored or coauthored more than 180 journal articles and 450 conference papers in his field, and eight books, holds seven international patents, and organized several tutorials at international conferences. He has worked on many projects for the industry concerning wind and wave energy, power electronic applications for power systems, such as Smarttrafo; HVDC systems, projects for smart cities such as photovoltaic (PV) charging of electric vehicles, PV and storage integration, contactless charging; and he participated in several Leonardo da Vinci and H2020, and Electric Mobility Europe EU projects as a Project Partner (ELINA, INETELE, E-Pragmatic, Micact, Trolley 2.0, OSCD, P2P, and Progressus) and a Coordinator (PEMCWebLab.com-Edipe, SustEner, Eranet DCMICRO).

Dr. Bauer is the Former Chairman of Benelux IEEE Joint Industry Applications Society, Power Electronics and Power Engineering Society Chapter, the Chairman of the Power Electronics and Motion Control Council, a Member of the Executive Committee of European Power Electronics Association, and also a Member of the International Steering Committee at numerous conferences.